GSA Data Repository 2016089

Shelfal sediment transport by an undercurrent forces turbidity-current activity during high sea level, Chile continental margin

Anne Bernhardt[1], Dierk Hebbeln[2], Marcus Regenberg[3], Andreas Lückge[4], and Manfred R. Strecker[1]

[1]Earth and Environmental Sciences, Universität Potsdam, Karl-Liebknecht-Strasse 24-25, 14476 Potsdam, Germany

[2]MARUM-Center for Marine Environmental Sciences, Bremen University, Bremen, Germany

[3]Institute of Geosciences, Christian-Albrechts-Universität, Kiel, Germany

[4]Federal Institute for Geosciences and Natural Resources, Hannover, Germany

Core	Latitude	Longitude	Water Depth (m)	Sediment recovery (m)	Cruise	References
North-central Chile						
GeoB 7136-2	-29.7167	-72.0662	3188	7.4	SO 156	Bernhardt et al., 2015a
GeoB 7138-2	-30.1332	-71.8688	2733	6.4	SO 156	Bernhardt et al., 2015a
GeoB 3368-2	-30.3600	-71.9583	3238	4.6	SO 156	Bernhardt et al., 2015a
GeoB 3369-1	-30.0433	-72.0167	3457	5.5	SO 156	Bernhardt et al., 2015a
GeoB 3304-5	-32.8900	-72.1917	2411	9.1	SO 156	Bernhardt et al., 2015a
South-central Chile						
SL 21	-36.1188	-73.8142	2468	9.5	SO 161	Bernhardt et al., 2015a
SL 113	-36.9732	-74.1667	3187	4.8	SO 161	Bernhardt et al., 2015a
SL 112	-38.0808	-74.4968	4125	5.7	SO 161	Bernhardt et al., 2015a
GeoB 9802	-36.5833	-74.5834	4822	1.7	SO 181	Heberer et al., 2010; Bernhardt et al., 2015b
GC 14	-36.6333	-73.7625	1822	5.8	SO 210	Völker et al., 2011; Bernhardt et al., 2015b
SL 50	-38.3125	-74.6975	4380	9.1	SO 161	Blumberg et al., 2008
ODP 1232	-39.8908	-75.9013	3187	470	Ocean Drilling Program Leg 202	Blumberg et al., 2008

Table DR1. Sediment cores selected for this study.

Chile margin morphology and core locations

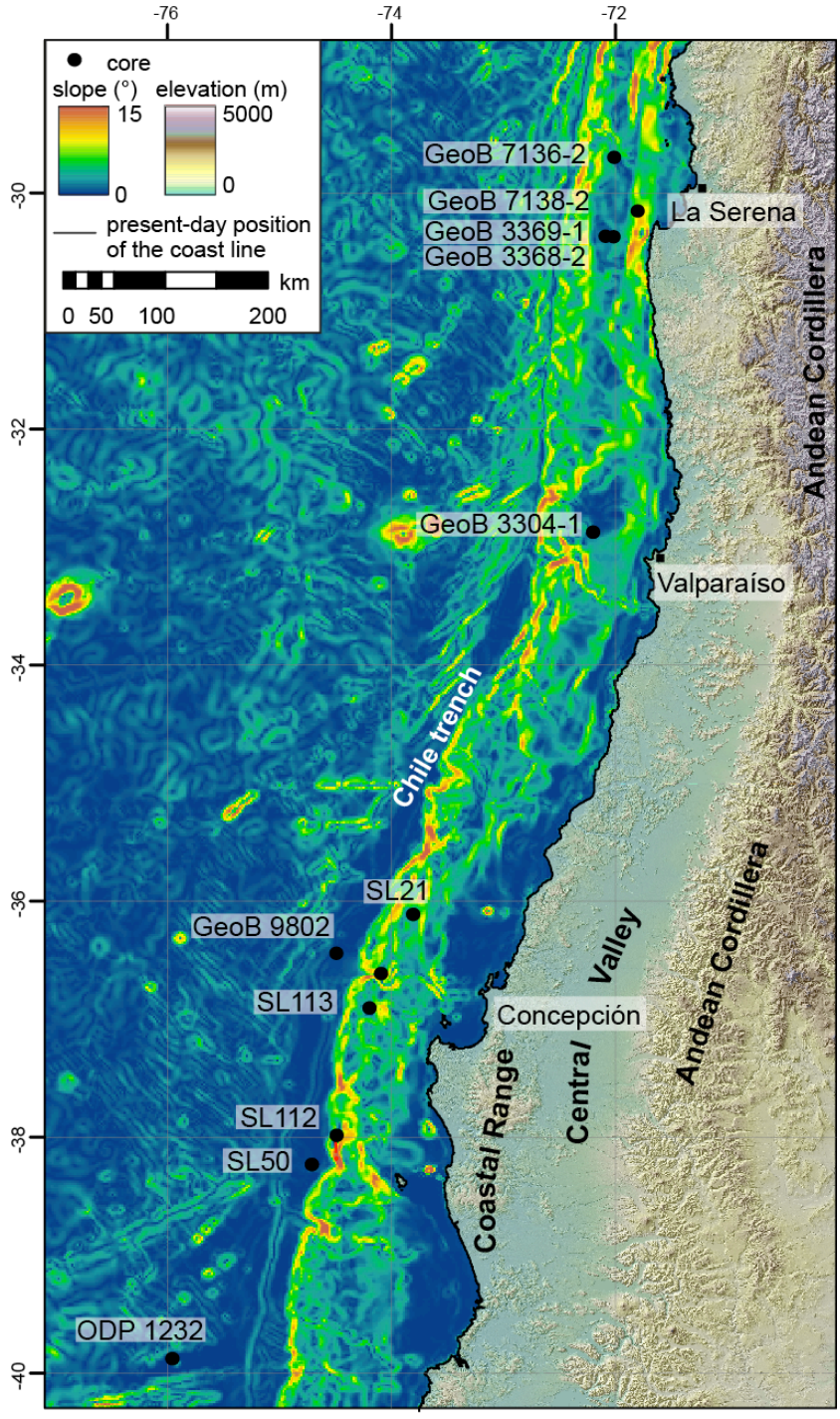

Figure DR1. Overview view map showing an offshore slope map computed from the publically available Etopo1 dataset (1 arc minute grid; http://www.ngdc.noaa.gov/mgg/global/) and the onshore relief derived from the Shuttle Radar Topography Mission (SRTM). Note the steep coast-proximal slope close in north-central Chile (29-33°S) in comparison to a shallow dipping and relatively wide shelf offshore south-central Chile (36-40°S).

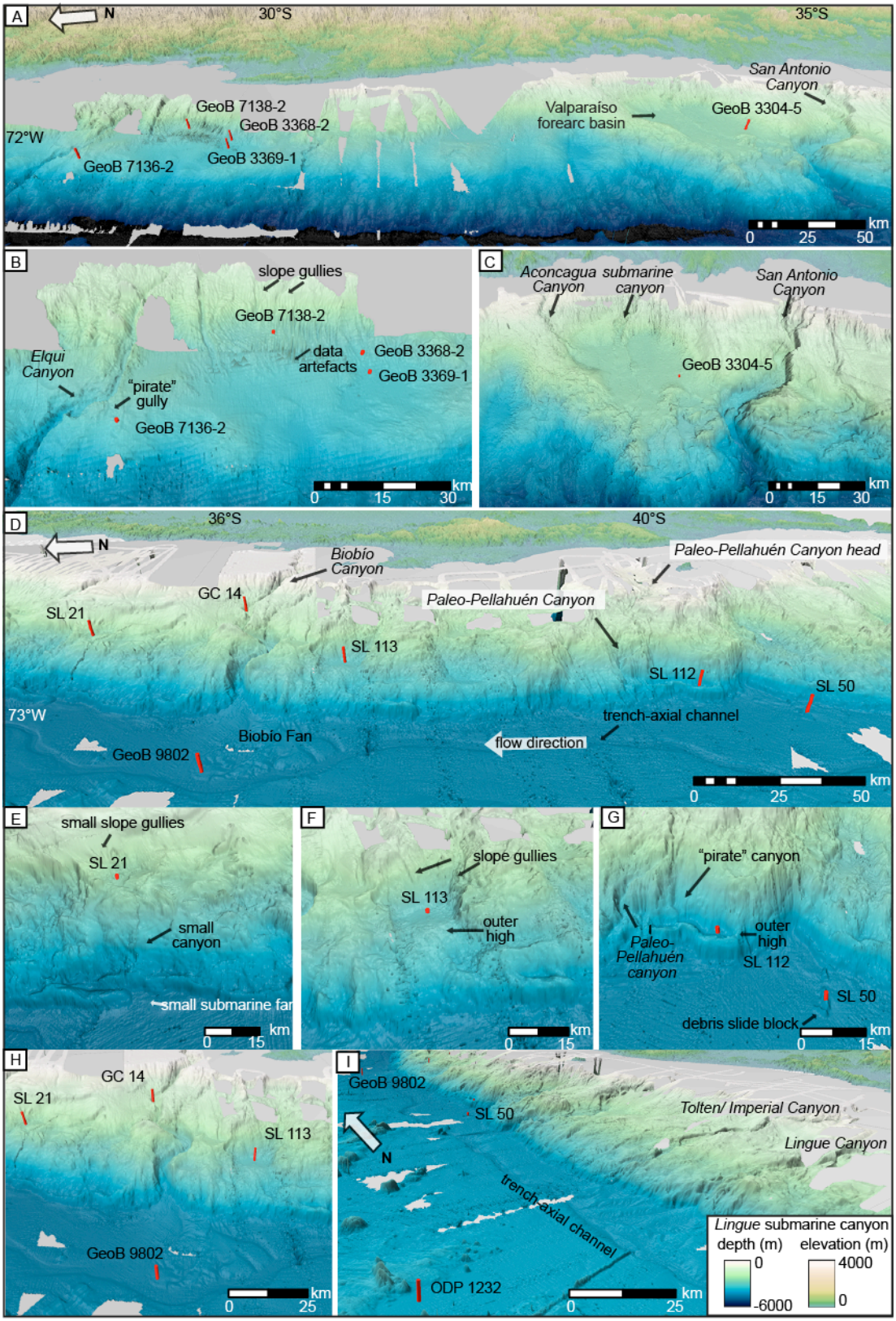
A
N
30°S
35°S
72°W
GeoB 7138-2
GeoB 3368-2
GeoB 3369-1
GeoB 7136-2
Valparaíso
forearc basin
San Antonio
Canyon
GeoB 3304-5
km
0 25 50
B
slope gullies
GeoB 7138-2
Elqui
Canyon
data
artefacts
GeoB 3368-2
GeoB 3369-1
"pirate"
gully
GeoB 7136-2
km
0 15 30
C
Aconcagua
Canyon
submarine
canyon
San Antonio
Canyon
GeoB 3304-5
km
0 15 30
D
36°S
40°S
N
Biobío
Canyon
Paleo-Pellahuén Canyon head
GC 14
Paleo-Pellahuén Canyon
SL 21
SL 113
SL 112
SL 50
73°W
trench-axial channel
Biobío Fan
flow direction
GeoB 9802
km
0 25 50
E
small slope gullies
SL 21
small
canyon
small submarine fan
km
0 15
F
slope gullies
SL 113
outer
high
km
0 15
G
"pirate" canyon
outer
high
Paleo-
Pellahuén
canyon
SL 112
SL 50
debris slide block
km
0 15
H
GC 14
SL 21
SL 113
GeoB 9802
km
0 25
I
GeoB 9802
SL 50
N
Tolten/ Imperial Canyon
Lingue Canyon
trench-axial channel
ODP 1232
km
0 25
Lingue submarine canyon
depth (m)
elevation (m)
0
-6000
4000
0

Fig. DR2. A) Detailed three-dimensional view of the bathymetry offshore Chile showing the core locations. B) In the north four cores have been taken from small intraslope basins. GeoB 7136-2 is located on the flanks of a submarine canyon. C) GeoB 3304-5 is located within the Valparaiso forearc basin. D, E) In the south, SL21 was recovered from a 10 x 4.5 km slope basin drained by a lower slope gully. F) The SL113 core site is located in an 18 x 11 km enclosed basin and G) SL112 was cored in a 16 x 4 km, enclosed basin that is connected via a small pirate canyon to the larger paleo-Pellahuén Canyon. The canyon head is located about 30 km westward of the present-day shoreline at -200 m. SL50 is located within the trench and atop a 400 m-high debris block. H) GeoB 9802 is located on the distal fringe of the Biobío submarine fan. GC 14 was recovered from an in-canyon terrace. I) ODP 1232 is located on the incoming plate. Elevation is 6 times exaggerated (modified and amended from Bernhardt et al., 2015a).

Oxygen Isotopes

Oxygen isotopes were measured in cores SL21, GeoB3304-5, GeoB3369-1, and GeoB7138-2. For the measurements ~40 specimens of *G. bulloides* were crushed and homogenized, cleaned in ethanol in an ultrasonic bath and dried at 40 °C. Double measurements of the powder were performed and mean values were calculated. Measurements were run on a Finnigan MAT251 Mass Spectrometer with automated Kiel carbonate preparation device (Type I) at Leibnitz Laboratory for Radiometric Dating and Stable Isotope Research, University of Kiel. Samples were reacted with 99% phosphoric acid at 73 °C. The standard external error is better than 0.07‰. Replicate measurements indicate a mean $d^{18}O$ standard deviation of 0.09‰ (n=11). Calibration to the Vienna Pee Dee Belemnite (V-PDB) scale was performed via the National Bureau of Standards (NBS) 18, 19 and 20.

Radiocarbon Dating and Calibration

Three new radiocarbon ages were obtained for SL21, to refine the mid to late Holocene age model for the core (Table DR2). Marine radiocarbon ages were calibrated to calendar years by calculating the probability distribution of the samples true age using the Calib 7.0 software employing the MARINE 13 calibration curve (Reimer et al., 2013). Ages were corrected for a reservoir age of 370 ± 51 years according to a measurement by Ingram and Southon (1996) who investigated the reservoir age by analyzing a pre-bomb bivalve Mytilus californianus collected in 1939 offshore Valparaiso. Hence, no significant deviation from the global reservoir effect of ~400 years is assumed. For ODP Site 1233 at 41°S (Strub et al., 1998), the assumption of a 400-yr reservoir age appears to be reasonable because a volcanic ash layer interpolated radiocarbon age of ~9,600 years correlates to a regionally recorded tephra layer onshore with an independently dated age close to 9,500 ^{14}C years B.P. (Lamy et al., 2004). Additionally, De Pol-Holz et al. (2010) compiled a δO^{18} record for SL22, a core acquired during Sonne cruise SO-161 at 36°13'S and 73°40'W, located 41 km north of the GC14 and the BioBío Canyon. These authors also assume a 400 yr reservoir effect due to the timing of the deglacial changes in the planktonic δO^{18} record of SL22 and its similarity with the Antarctic ice-core δO^{18} record, when a 400 yr reservoirs age correction is applied. However, it is important to recognize that

temporal variability of the reservoir ^{14}C age could have limited the accuracy of ^{14}C chronology.

Core	core depth (m)	Lab. No.	14C age yr BP	14C age yr error	61 % (1s) cal age ranges (yrs)		95.4 % (2s) cal age ranges (yrs)		median probability cal BP	relative area under distri-bution	material dated
					lower	upper	lower	upper			
SL 21	8.31-8.34	Poz-62382	4710	60	5293	5591	5047	5745	**4884**	1	mixed planktonic foraminifera
SL 21	8.47-8.49	Poz-62383	5160	130	5256	5738	4942	5932	**5445**	1	mixed planktonic foraminifera
SL 21	8.87-8.89	Poz-62386	4850	80	4945	5222	4832	5293	**5069**	1	mixed planktonic foraminifera

Table DR2. Newly acquired radiocarbon ages and their calibration for core SL21.

Age Reversals

One age reversal was identified in the newly acquired radiocarbon ages of SL21 but ages are equivalent between 2σ errors (Table DR2). Statistical age modeling requires monotonically increasing ages from top to bottom of the section (e.g. Blaauw and Christen, 2011; Trauth, 2014). Therefore, the age of these two layers were edited within the 2σ errors range of the radiocarbon ages to 5250 kyr BP and 5280 kyr BP (e.g., Trauth, 2014)

Age Modeling

A probabilistic age modeling technique of Trauth (2014) that accounts for abrupt changes and extreme variations in sedimentation rates is employed. The algorithm provides independent means of determining the position and temporal length of even small-scale hiatuses by the evaluation of the overlap of two independent age distributions, one derived from characteristic sedimentation rates for each sediment type and one derived by the age differences of the radiocarbon ages throughout the section. In sediment cores dominated by turbidite sedimentation and hemipelagic settling of clay, sedimentation rates vary tremendously from several millimeters per second for turbidite sands (e.g., Sumner et al., 2008) to a few millimeters per 1000 years for the hemipelagic material. Frequent hiatuses in deposition are highly likely in these marine clastic successions, because turbidity

currents are often erosive and may first erode some of the underlying section and then deposit their load.

The Gamma model for the most likely unit deposition time, the inverse of the sedimentation rate, for each sediment type is defined by two parameters, shape and scale. In the experiments described here, a Gamma model with shape = 2 best describes the frequency distribution of unit deposition times, which is in agreement with the work of Blaauw and Christen (2011).

The defined sediment types are (1) Holocene hemipelagic mud, (2) turbiditic mud. No sand is present in core SL21. Scale factors of each sediment type mirror the unit deposition times (yr/mm). The agreement between the independent estimates of time accumulated in the sediment based on unit deposition time and age differences between calibrated radiocarbon ages is expressed as the percentage overlap of the two distributions (indicated in green in the age model plot). The age model is calculated based on 5 mm-thick core slices. The reader is referred to the supplementary material of Bernhardt et al. (2015a) for details of the age modeling technique and models.

SL21 age model

Scale factors of 1 for sediment type 1 and 0.26 for sediment type 2 are used to obtain a good match between the time accumulated based on sedimentation rates and the age differences between radiocarbon ages. Age modeling suggests that the around 160 yrs cal BP (in total 212 yrs, 160 BP + 52 yrs up till 2002) are missing at the core top (Fig. DR6). Due to the large error bar associated with the oldest age of the core and the possibility of a hiatus in that section, we excluded the section older than 5.5 kyr cal BP from our investigation.

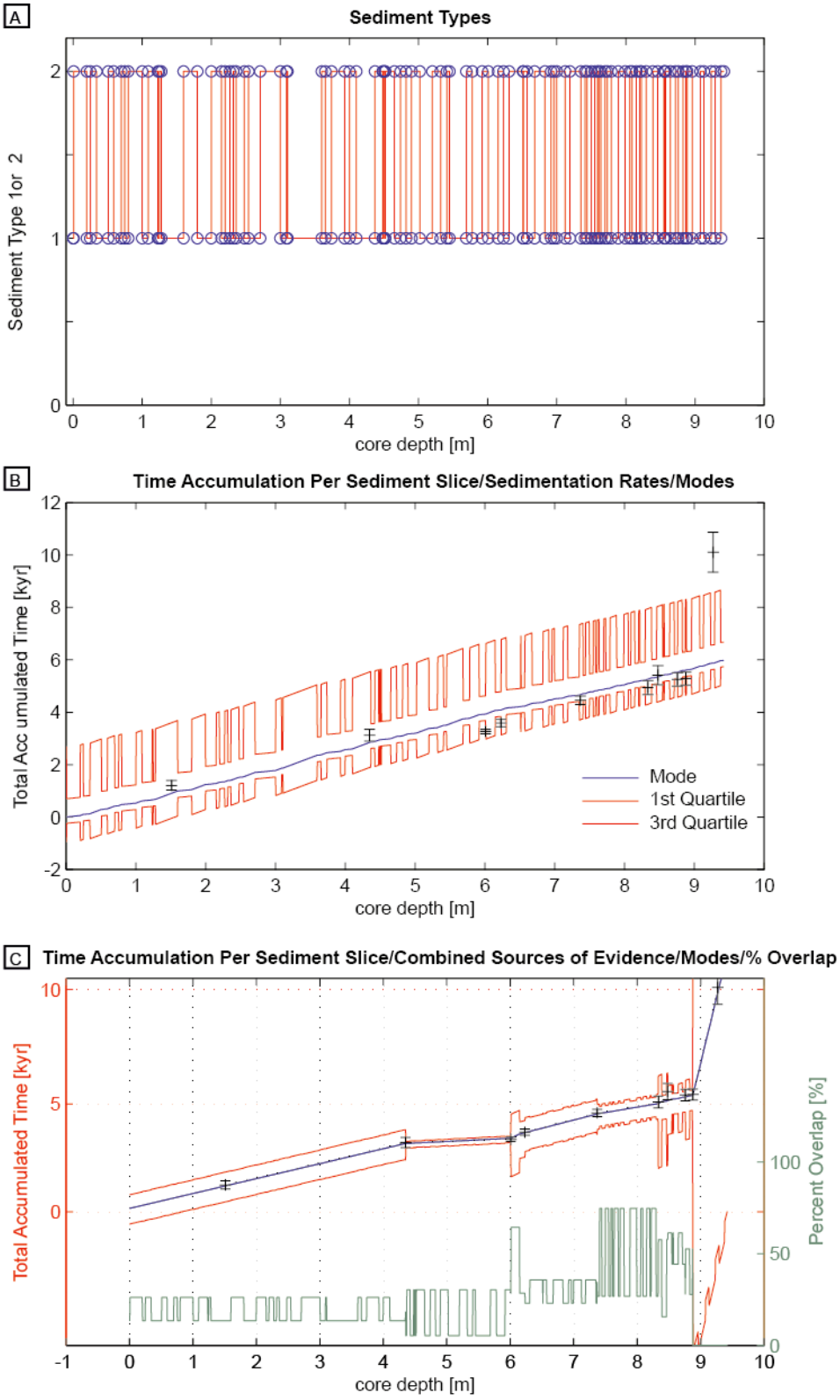

Figure DR3. Revised age model for core SL21 (with data from Bernhardt et al. (2015a). A) Core depth vs. sediment type for SL21. The defined sediment types are (1) Holocene hemipelagic mud and (2) turbiditic mud and silt. B) Time accumulated per sediment slice (5 mm) based on the average sedimentation rates of the two sediment types for SL21. C) Finalized age model for SL21, including a core section equivalent to ~ 160 yrs cal BP missing at core top.

Turbidite Identification

In the north-central Chile, turbidites can be easily identified visually due to a pronounced color difference between turbidites and hemipelagic clay and were confirmed by magnetic susceptibility measurements (Fig. DR4A). Turbidites were identified based on the fining-upward texture of the individual layers and the presence of Bouma-divisions. In the south-central Chile, turbidites are mud-rich and there is no pronounced color difference between hemipelagic clay intervals and turbidite mud. Hence, visual identification of turbidites is based on X-radiographs (Fig. DR4B). X-radiographs were taken of 1-cm-thick sediment slices sealed in plastic boxes of 20 cm length and 10 cm width. A Philips 80KV energy source was used, mounted at a distance of 1.2 m above the sample; the radiographs were fabricated of Agfa D4 Structurix film using an exposure time of 30 sec. The film negatives were scanned at high resolution with a standard PC scanner and then color-inverted with a standard graphic program. The resulting x-radiographs reveal high-resolution images of internal sediment structures. Light-colored sections of the photographs are related to sediment layers with high density and/or coarse sediment components, whereas gray and dark sections depict homogenous hemipelagic mud. Where necessary, turbidite thickness was confirmed by magnetic susceptibility measurements acquired with a GEOTEK Multi-Sensor Core Logger (Fig. DR4).

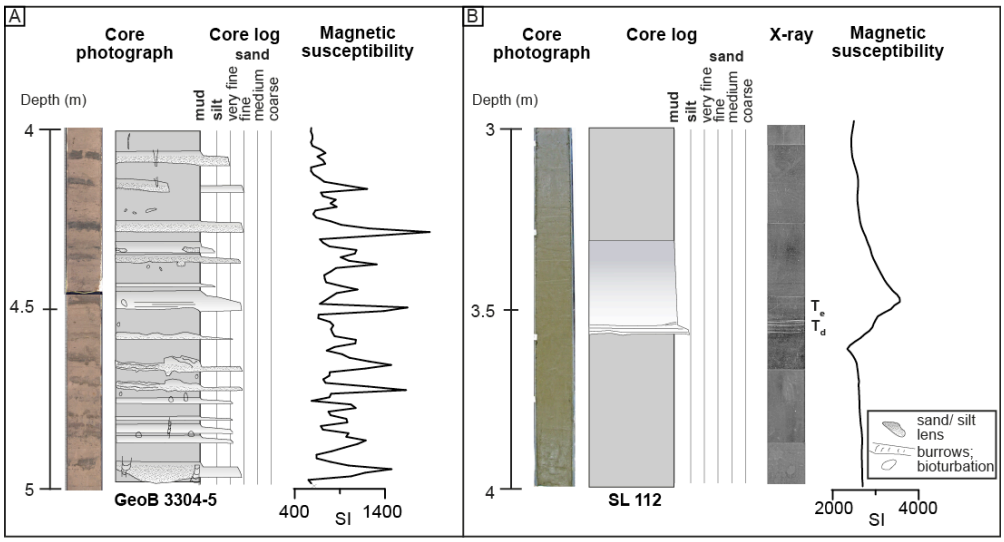

Figure DR4. Turbidite recognition in an examplary core of A) the north-central Chile where turbidites can be dentified visually and B) the south-cental Chile, where turbidites are predominantly muddy and were identified with the help of X-radiographs and magnetic susceptibility measurements. The X-radiograph shows a silty-muddy T_d (plane lamination) and T_e divisions of the Bouma-Sequence. Magnetic susceptibility increases due to an increased portion of terrestrial sediment.

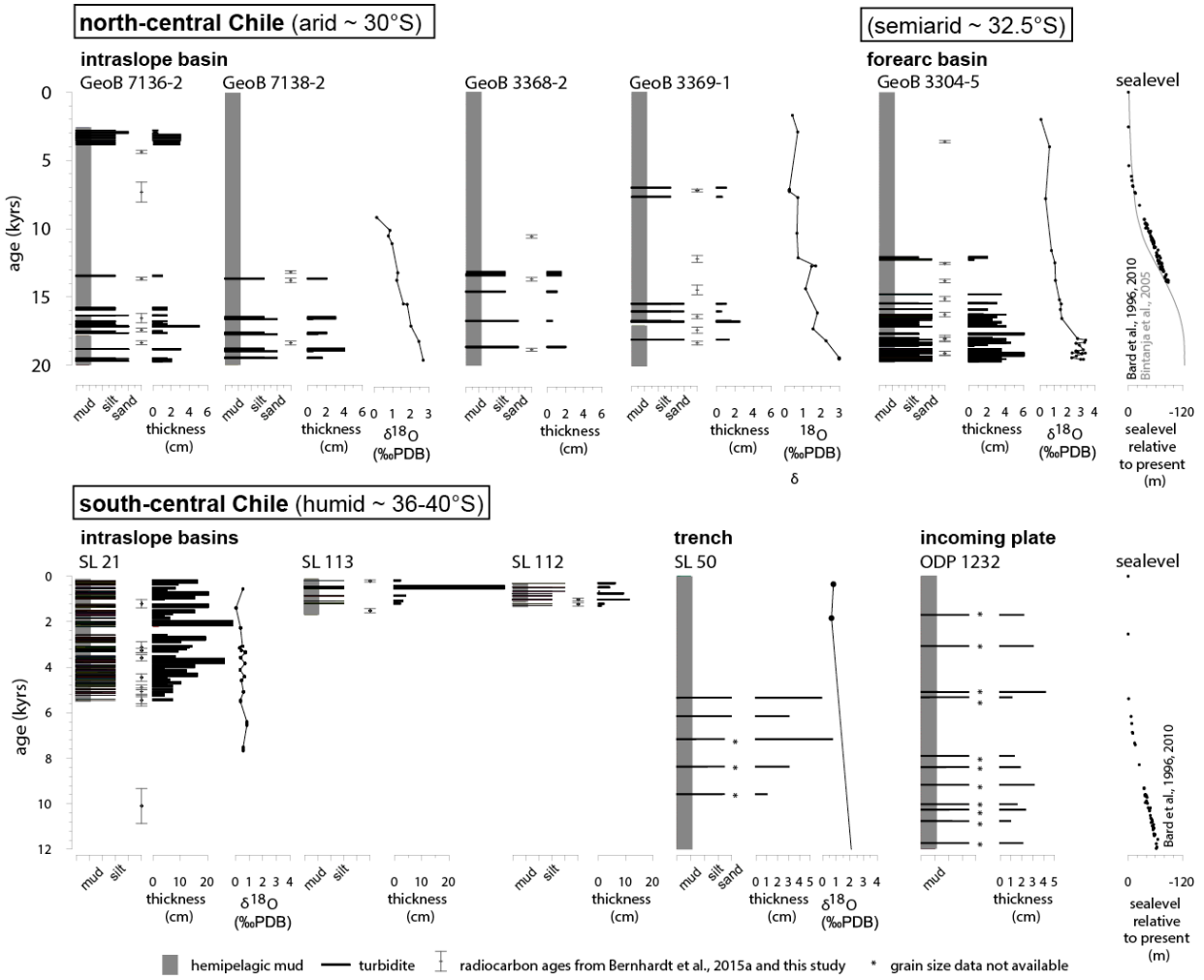

Figure DR5. Turbidite record of the individual cores. The turbidite record of SL50 and ODP 1232 was compiled by Blumberg et al. (2008). Sealevel curves from (Bard et al., 1996; 2010; Bintanja et al., 2005)

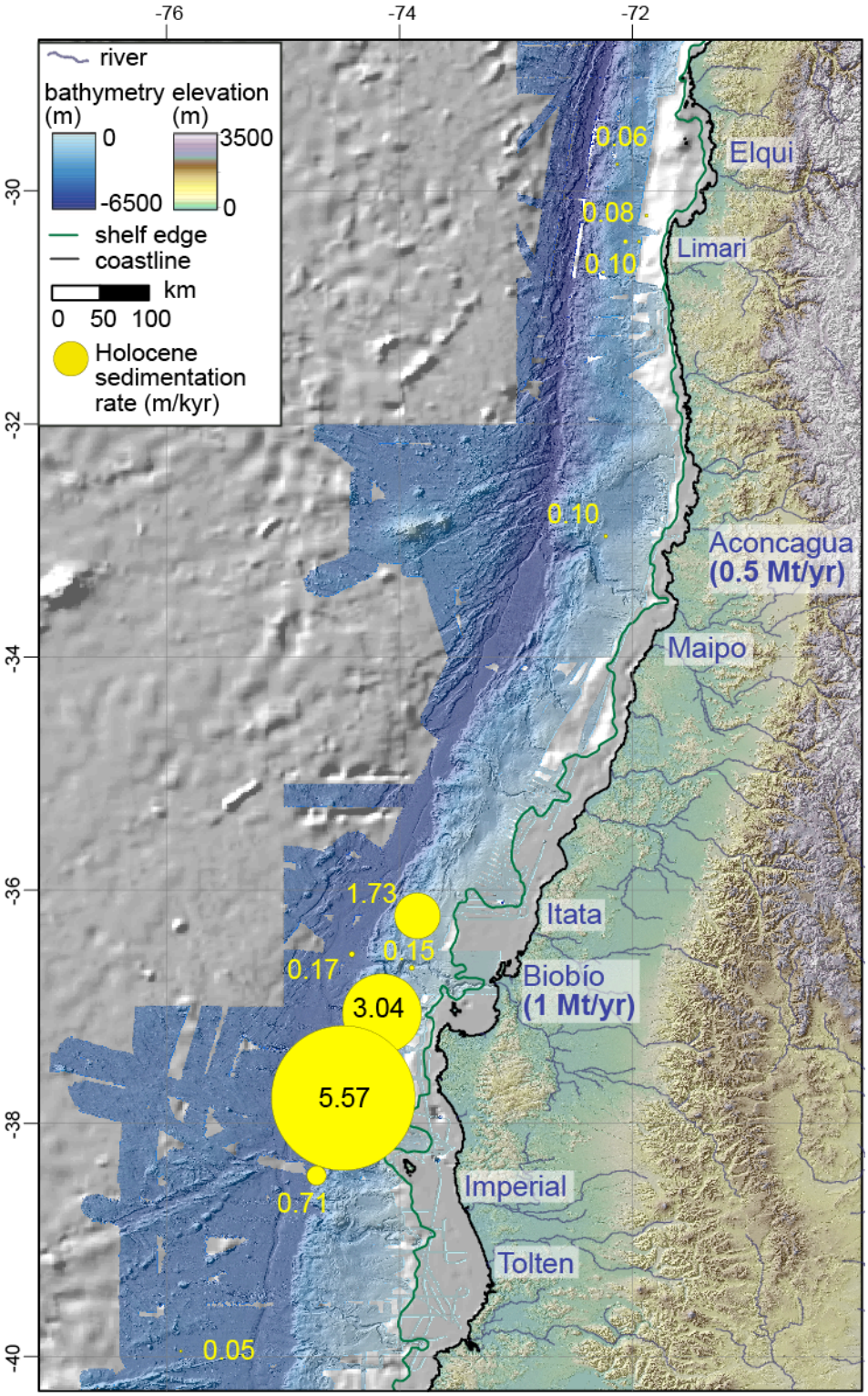

Figure DR6. Overview view map showing the offshore bathymetry and the onshore shaded relief map (SRTM 90m). Yellow bubble plots visualize Holocene sedimentation rates from core sites. The mean annual suspended sediment load for the Aconcagua River (Milliman and Farnsworth, 2011) and the Biobío River (before damming, Tolorza et al., 2014) are indicated to illustrate enhanced fluvial sediment transport to the ocean in south-central Chile.

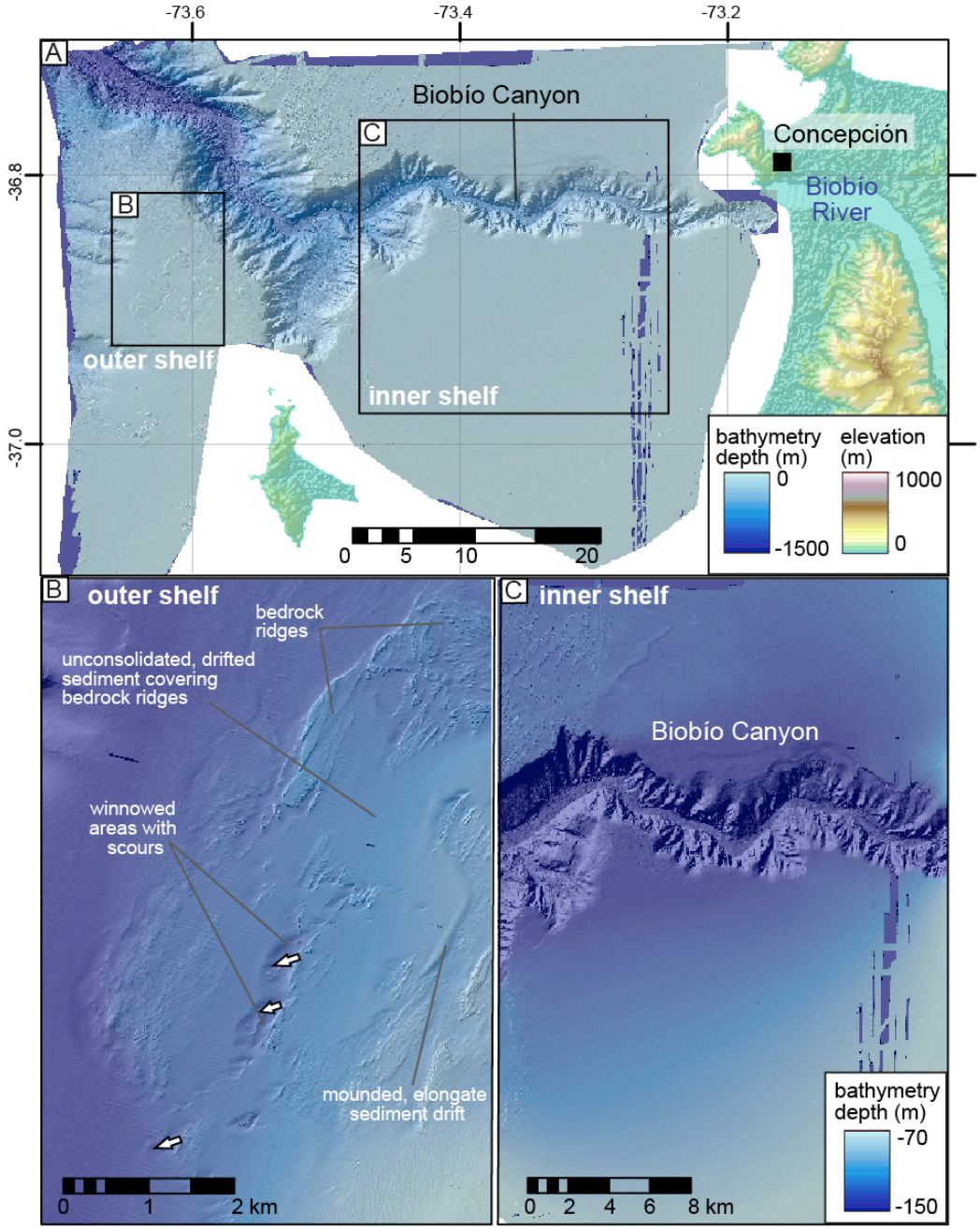

Figure DR7. High-resolution (5m grid-cell size) multibeam bathymetry offshore the city of Concepción and the Biobío River acquired by the Hydrographic and Oceanographic Service of the Chilean Navy (SHOA) in cooperation with the U.S. Naval Oceanographic Office in 2011 and previously published by Bernhardt et al. (2015b). The survey was conducted by the T-AGS 60 *Pathfinder* oceanographic survey vessel using Simrad EM710 and EM122 multibeam echosounders. A) The extent of the multibeam bathymetry survey of the shelfal part of the Biobío Canyon. Note the Biobío River-mouth to Canyon-head connection. B) Close to the shelf edge, the outer shelf displays rugged bedrock ridges with piles of unconsolidated sediment in between. The direction of erosional scours can be used as indicators for undercurrent direction **(white arrows)**. The Gunther undercurrent seems to transport loose sediment over the shelf edge in a south-southwestern direction. This process is inferred to dominate sediment export to the continental slope basins during Holocene sea-level highstand. C) The inner shelf appears smooth and covered by sediment. This part of the shelf is inferred to be unaffected by the Gunther undercurrent.

References

Bard, E., Hamelin, B., Arnold, M., Montaggioni, L., Cabioch, G., Faure, G., and Rougerie, F., 1996, Deglacial sea-level record from Tahiti corals and the timing of global meltwater discharge: Nature, v. 382, no. 6588, p. 241–244, doi: 10.1038/382241a0.

Bard, E., Hamelin, B., and Delanghe-Sabatier, D., 2010, Deglacial meltwater pulse 1B and Younger Dryas sea levels revisited with boreholes at Tahiti.: Science (New York, N.Y.), v. 327, no. 5970, p. 1235–1237, doi: 10.1126/science.1180557.

Bernhardt, A., Hebbeln, D., Lückge, A., Melnick, D., and Strecker, M.R., 2015a, Turbidite paleoseismology along the Chilean continental margin – feasible or not? Quaternary Science Reviews, v. 120, p. 71–92, doi: 10.1016/j.quascirev.2015.04.001.

Bernhardt, A., Melnick, D., Jara-Muñoz, J., Argandoña, B., González, J., and Strecker, M.R., 2015b, Controls on submarine canyon activity during sea-level highstands: The Biobío canyon system offshore Chile: Geosphere, v. 11, no. 4, p. 1–30, doi: 10.1130/GES01063.1.

Bintanja, R., van de Wal, R.S.W., and Oerlemans, J., 2005, Modelled atmospheric temperatures and global sea levels over the past million years.: Nature, v. 437, no. 7055, p. 125–8, doi: 10.1038/nature03975.

Blaauw, M., and Christen, J., 2011, Flexible paleoclimate age-depth models using an autoregressive gamma process: Bayesian Analysis, v. 6, no. 3, p. 457–474, doi: 10.1214/11-BA618.

Blumberg, S., Lamy, F., Arz, H., Echtler, H., Wiedicke, M., Haug, G., and Oncken, O., 2008, Turbiditic Trench Deposits at the South-Chilean Active Margin: A Pleistocene-Holocene Record of Climate and Tectonics: Earth and Planetary Science Letters, v. 268, p. 526–539, doi: doi:10.1016/j.epsl.2008.02.007.

Ingram, B., and Southon, J., 1996, Reservoir ages in Eastern Pacific coastal and estuarine waters: Radiocarbon, v. 38, no. 3, p. 573–582.

Lamy, F., Kaiser, J., Ninnemann, U., Hebbeln, D., Arz, H.W., and Stoner, J., 2004, Antarctic timing of surface water changes off Chile and Patagonian ice sheet response.: Science, v. 304, no. 5679, p. 1959–62, doi: 10.1126/science.1097863.

Milliman, J.D., and Farnsworth, K.L., 2011, River Discharge to the Coastal Ocean - A Global Synthesis: Cambridge University Press, Cambridge.

De Pol-Holz, R., Keigwin, L., Southon, J., Hebbeln, D., and Mohtadi, M., 2010, No signature of abyssal carbon in intermediate waters off Chile during deglaciation: Nature Geoscience, v. 3, no. 3, p. 192–195, doi: 10.1038/ngeo745.

Reimer, P., Bard, E., and Bayliss, A., 2013, IntCal13 and Marine13 radiocarbon age calibration curves 0–50,000 years cal BP: Radiocarbon, v. 55, no. 4, p. 1869–1887.

Strub, P.T., Mesias, J.M., Montecino, V., Ruttlant, J., and Salinas, S., 1998, Coastal ocean circulation off western South America, *in* Robinson, A.R. and Brink, K.H. eds., The Global Coastal Ocean: Regional Studies and Syntheses, John Wiley, New York, p. 273–315.

Sumner, E.J., Amy, L. a., and Talling, P.J., 2008, Deposit Structure and Processes of Sand Deposition from Decelerating Sediment Suspensions: Journal of Sedimentary Research, v. 78, no. 8, p. 529–547, doi: 10.2110/jsr.2008.062.

Tolorza, V., Carretier, S., Andermann, C., Ortega-culaciati, F., Pinto, L., and Mardones, M., 2014, Contrasting mountain and piedmont dynamics of sediment discharge associated with groundwater storage variation in the Biobío River: v. 119, no. 1, p. 2730–2753, doi: 10.1002/2014JF003105.Supply.

Trauth, M., 2014, A new probabilistic technique to build an age model for complex stratigraphic sequences: Quaternary Geochronology, v. 22, p. 65–71.